

Highlights

Gamma Ray Detection Efficiency of GAGG Crystal Scintillator Using Three Tagged Gamma Ray Techniques

B. Doty, N. Solomey, J. Folkerts, B. Hartsock, H. Meyer, M. Christl, M. Rodriguez-Otero, E. Kuznetsov

- We can determine a scintillator's absolute efficiency using radiation cascades.
- GAGG crystal scintillators are a promising target for a neutrino detector.
- GAGG scintillation detectors can be up to 92.8% efficient for gamma detection.

Gamma Ray Detection Efficiency of GAGG Crystal Scintillator Using Three Tagged Gamma Ray Techniques

B. Doty^{a,1,*}, N. Solomey^a, J. Folkerts^a, B. Hartsock^a, H. Meyer^a, M. Christl^b, M. Rodriguez-Otero^b, E. Kuznetsov^b

^a*Wichita State University, 1845 Fairmount St., Wichita, 67260, Kansas, United States of America*

^b*Marshall Space Flight Center, NASA, 320 Sparkman Blvd., Huntsville, 35812, Alabama, United States of America*

Abstract

A CubeSat with a prototype scintillating detector with a sensitive volume of GAGG crystal is being developed with a possible launch date of 2025. Its purpose is to characterize the background signals that mimic the neutrino interaction that the ν SOL team is looking for. An important part of the characterization of the backgrounds and the expected real signal is understanding the gamma ray detection efficiency of the prototype detector. To this end we have used and developed three techniques to do an absolute measurement of gamma ray efficiency. The first is using EC sources that emit an X-ray before prompt emission of a de-excitation gamma ray, specifically ^{65}Zn and ^{54}Mn . The second is using a β^+ decay source wherein a positron annihilates on an atomic shell electron producing two back-to-back 511 keV gammas followed promptly by a de-excitation gamma, specifically ^{22}Na . The third is using a gamma cascade of two near-simultaneous de-excitation gammas from the same nucleus, specifically from ^{60}Co decay.

Keywords: neutrino, gallium, GAGG, gamma, scintillating crystal, detector efficiency

*Corresponding Author

¹*Email:* bsdoty@shockers.wichita.edu

1. Introduction

The ν SOL project aims to detect solar neutrinos with a space-based detector featuring a Gallium-Aluminum-Gadolinium-Garnet (GAGG) scintillating crystal using the double pulse delayed coincidence of the ^{71}Ga neutrino absorption process [1]. When a solar neutrino interacts with ^{71}Ga , it promotes the nucleus to ^{71}Ge , which may be excited so long as the neutrino has sufficient energy to produce the excited state. This excited state decays via a 175 keV gamma ray [2], it is this gamma ray and the prompt electron that we aim to use as the neutrino identification technique. It is therefore critical that we understand the gamma ray detection efficiency of the GAGG detector.

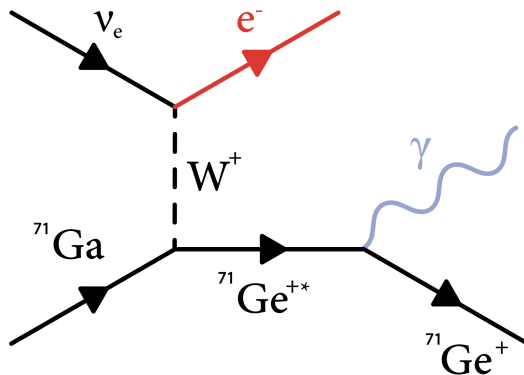


Figure 1: The relevant neutrino interaction to detect solar neutrinos. The ^{71}Ga nucleus interacts with the electron neutrino to produce an excited state of ^{71}Ge , which then subsequently decays via a gamma ray.

The overall mission has 2 stages. The second stage is a solar probe with many kilograms of GAGG being launched into a highly elliptical orbit with a closest approach of approximately 7 solar radii, following in the footsteps of Parker Solar Probe. It is this stage that will actually have a chance at detecting solar neutrinos. The first stage, in contrast to a large solar probe, is a 3U CubeSat with about 73 grams of GAGG that is launched into a polar orbit where the earth's magnetic shielding effect is small and so the detector will be exposed to background events that are expected to be similar to the backgrounds the eventual solar probe will experience. This detector will not detect a solar neutrino, but will give a real look into the backgrounds that could potentially interfere with the neutrino reconstruction process.

We have determined the gamma detection efficiency for the CubeSat flight detector, which is a 2x2 array of GAGG crystals each 14X14X14 mm with a single quartz light guide that is 28x28x10mm and 16 silicon photo multipliers (SiPMs) on the quartz. There is optical resin between each of the GAGG and quartz surfaces.

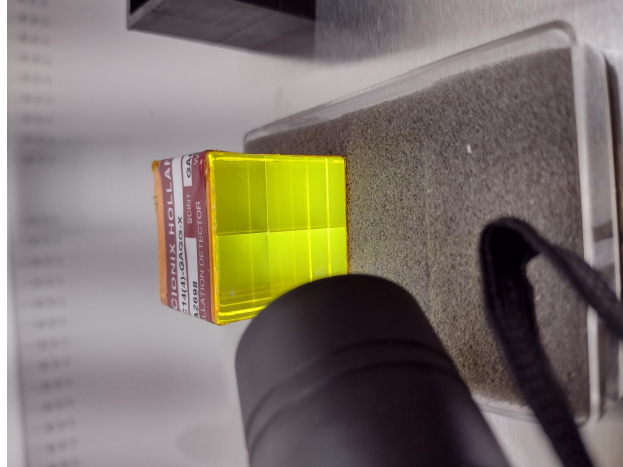


Figure 2: The array of GAGG crystals under UV light. This is before the bonding with SiPMs and the side facing the viewer is the quartz light guide.

2. Experimental Technique and Equipment

2.1. Triggered Gamma Ray Sources

To determine the gamma detection efficiency of a prototype detector, we must first know whether or not a gamma was even available to be detected. To do this, we use a triggered gamma ray source. This could be an X-ray triggered gamma source, an annihilation-triggered gamma source, or a gamma-triggered gamma source. We use an X-ray detector to trigger on one of the X-rays or gammas and look for the corresponding gamma in the flight detector, opposite to a similar absolute X-ray detection efficiency study [3]. For X-ray triggered gamma sources, both ^{65}Zn and ^{54}Mn undergo an electron capture (EC) of one of the atomic orbital electrons, which results in the emission of an X-ray, see figure 3. After electron capture, the resultant nucleus is in an excited state with a known probability, it is this gamma from the excited nucleus that we look for in the prototype detector.

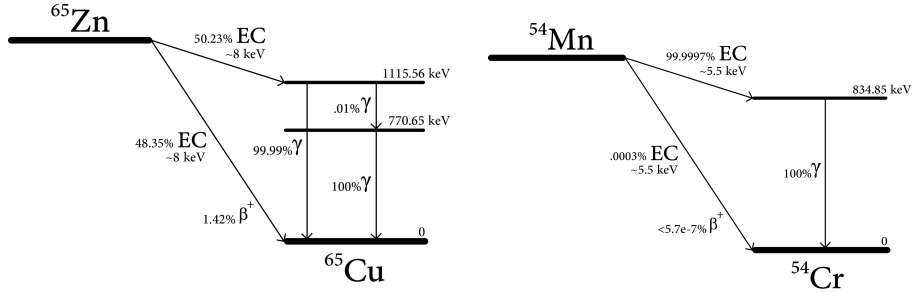


Figure 3: On the left is the ^{65}Zn electron capture decay chain. On the right is the ^{54}Mn electron capture decay chain.

We can also use gamma-triggered gamma sources where the trigger is made from a gamma ray, either by an annihilation gamma or a gamma cascade; ^{22}Na and ^{60}Co are both viable for this technique as they both have multiple coincident gammas that can be used for an efficiency measurement. In the case of ^{22}Na we used one of the 511 keV annihilation gammas to look for the 1274 keV gamma and the case where both the 1274 keV and 511 keV interact, which will hereafter be referred to as the combined peak. In the case of ^{60}Co we can use either gamma ray as a trigger to look for the other gamma, though some care needs to be taken to avoid the Compton scattering backgrounds since the two gammas are so close in energy.

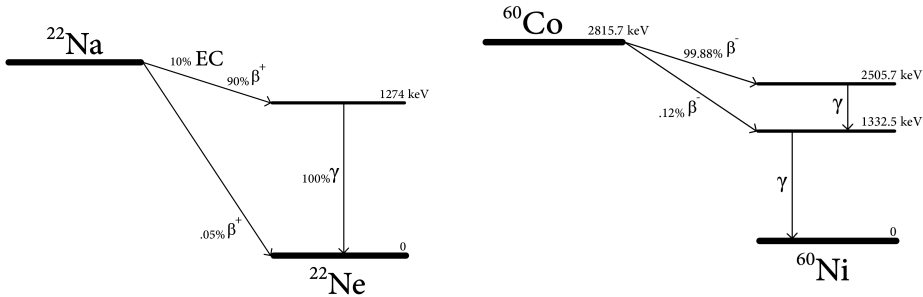


Figure 4: On the left is the ^{22}Na decay chain. On the right is the ^{60}Co decay chain.

2.2. Trigger Detector

The X-ray detector, $51\phi \times 10 \text{ mm}^3$, that is used as a trigger for this experiment is a Scionix detector that features a CeBr_3 crystal with a high light yield and a 0.3mm thick beryllium entrance window having a 250 ps FWHM

resolving time. This composition makes it suitable for detecting X-rays down to 5 keV and gamma rays up to about 2 MeV (containment limited by the 10 mm thickness).

2.3. Experimental Setup

For each detector and for each run the following overall setup is used: First, the source is taped directly to the X-ray detector, making sure that the side that is permeable to X-rays is facing the beryllium entrance window. Then, the combined source and X-ray detector is then brought as close as possible to the prototype detector in a manner that is reproducible. Lastly, a differential discriminator is used to trigger on the X-ray signal. This allows us to select the relevant energy regime for triggering on the X-ray and remove the vast majority of signals that would otherwise trigger an event. For comparison of the simulated detector to the real lab setup, see Figures 5 & 6.



Figure 5: The flight detector (bottom) and the X-ray detector (top) with a source in between them.

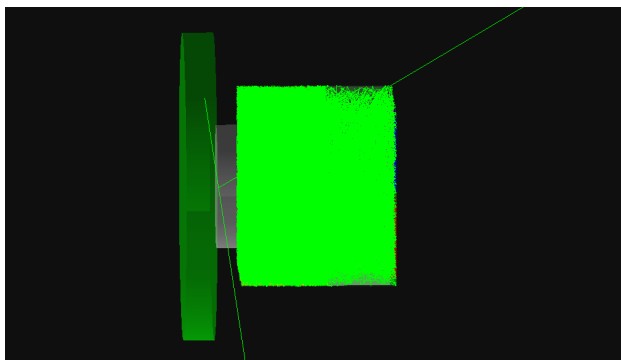


Figure 6: A visualization of the Geant4 simulation used to calculate the efficiency of the GAGG detector. The blue cylinder is the X-ray detector, the first 14mm of the large cube are the 4 GAGG crystals, then 10mm of quartz window with the 4 SiPMs on the end of the quartz, and finally the grey disk is the plastic source with a small deposit embedded at the end. Shown is a ^{22}Na decay with a positron annihilation and gamma de-excitation.

2.4. Data Acquisition Methods

We used an oscilloscope as our data acquisition method for both the GAGG prototype detector and the X-ray detector. For both detectors we took the integral of the waveform over time and the resulting integral is the value used for that event.

We then used ROOT [4] to generate histograms of these values and from integrating over the fit function corresponding to the X-ray or gammas we determine the number of X-rays detected by the X-ray detector and the number of gamma rays detected by the prototype detector.

3. Simulations

3.1. Simulation Overview

To measure the efficiency of the prototype detector, we used simulations to determine the portion of gamma rays that were emitted by the source that actually interact with the detector to produce a signal. Simulations of the prototype detectors were done in Geant4 [5] [6] [7] to determine the expected portion of emitted gamma rays.

The Geant4 simulation takes into account the scintillation yield as a function of wavelength for the scintillating material and optical photon counting in the SiPM including the quantum efficiency of the SiPM as a function of wavelength. The relevant source is modeled as a small disk that emits gamma

rays isotropically at each point of the disk and further embedded in a plastic disk. See Figure 6 for a view of the detector geometry.

Under these considerations, an interacting gamma ray in the simulated detector produces an optical photon count distribution that closely resembles the measured distribution of SiPM signal peaks in the real detector.

3.2. Simulation of Flight Detector

The simulated triggers were created using a logic surface that mimics the X-ray detector, this can be used to select for events that meet the criteria we choose. These simulated triggers were used to determine the correction factor for the ^{22}Na signals and the ^{60}Co signals. The ^{65}Zn and ^{54}Mn expected gamma values were calculated by simply spawning in an isotropic gamma ray source of the known energy, this matched the round of simulations with the logic source very closely.

The most important result from the simulation is the number of optical photons counted by the SiPMs (the simulated signal). These simulated signals look like the standard gamma signals with a Compton scattering region and a full energy deposition region, see Figure 7. We use ROOT to fit a Gaussian function to the histogram of optical photons, and integrate over the fit parameters to determine the number of gammas that are expected to be seen with a full energy deposit in the real detector. The portion of full energy deposits out of the total gammas produced is dubbed the correction factor. Note that this is without the branching fraction as that is kept as a separate factor for consistency.

Table 1: The correction factors obtained by Geant4 simulation along with the relevant branching ratios for the interaction considering the trigger. (Values over 99% are considered 100%)

Source	Energy	CF	BR
^{65}Zn	1115 keV	4.00%	50.23%
^{54}Mn	835 keV	5.60%	100%
^{22}Na	1274 keV	2.03%	200%
^{22}Na	1785 keV	0.69%	100%
^{60}Co	1173 keV	3.79%	100%
^{60}Co	1333 keV	3.28%	100%

A summary of the results of these simulations can be found in Table 1.

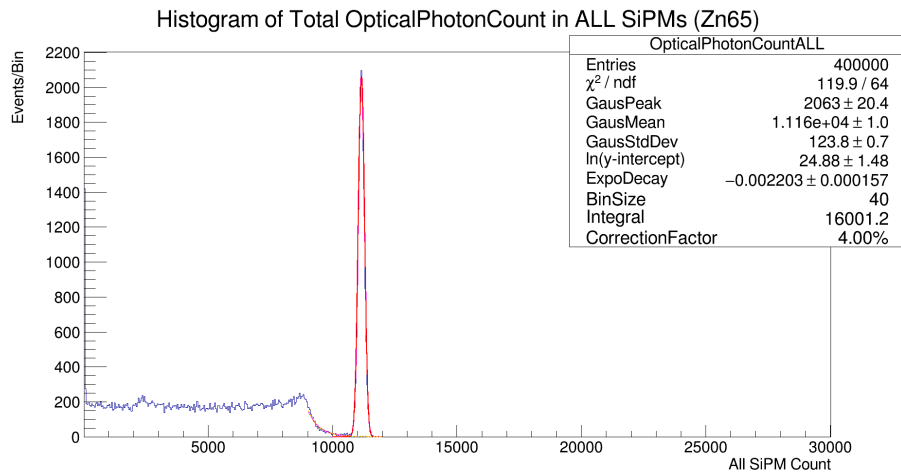


Figure 7: Simulated ^{65}Zn 1115 keV gamma interacting with GAGG detector.

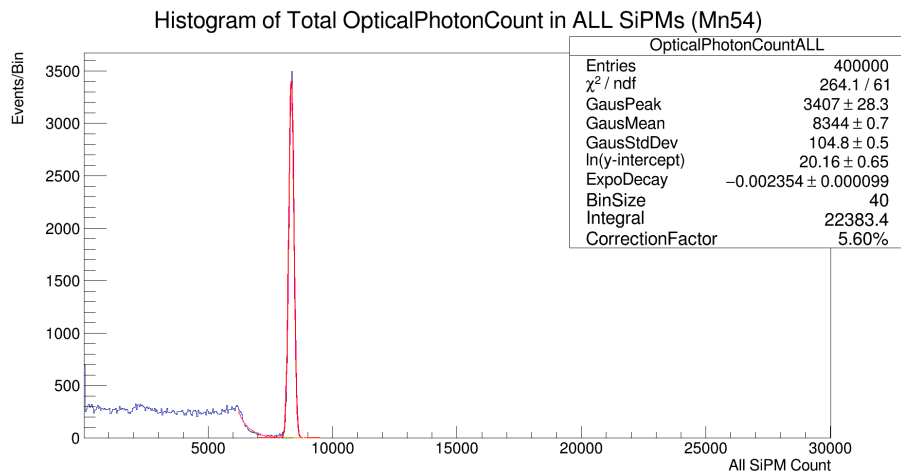


Figure 8: Simulated ^{54}Mn 835 keV gamma interacting with GAGG detector.

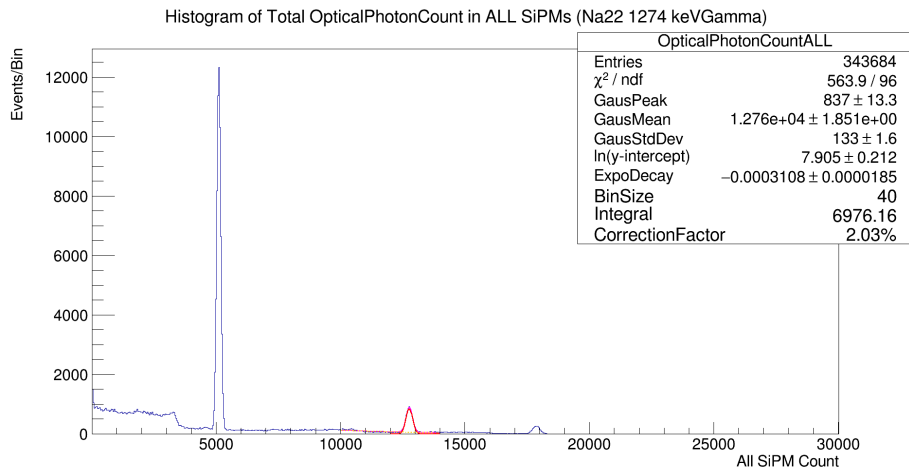


Figure 9: Simulated ^{22}Na decays with X-ray logic triggering on one of the 511 keV annihilation gammas. The fit is for the 1274 keV gamma interacting with the GAGG detector.

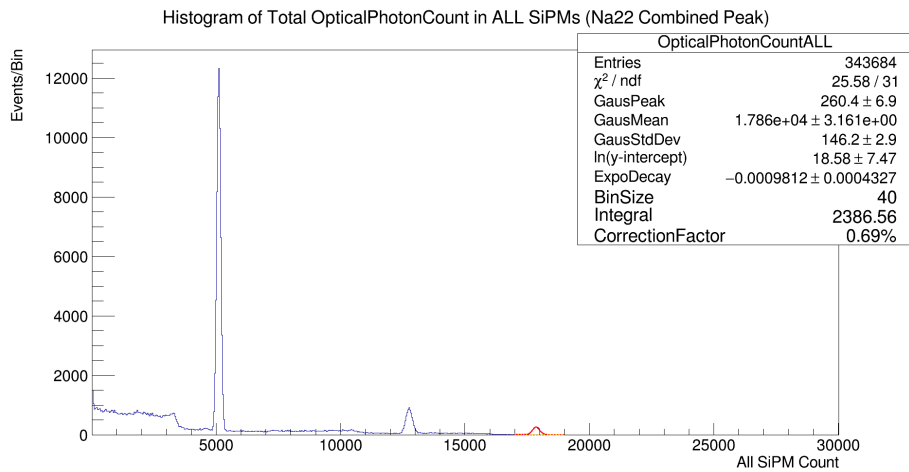


Figure 10: Simulated ^{22}Na decays with X-ray logic triggering on one of the 511 keV annihilation gammas. The fit is for the combined peak of both the 1274 keV gamma and one of the 511 keV annihilation gammas.

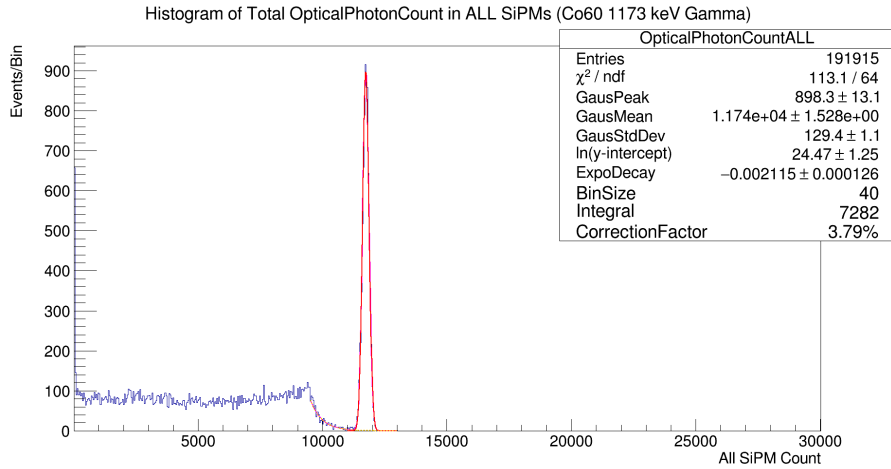


Figure 11: Simulated ^{60}Co 1173 keV decays with X-ray logic triggering on the 1333 keV gamma.

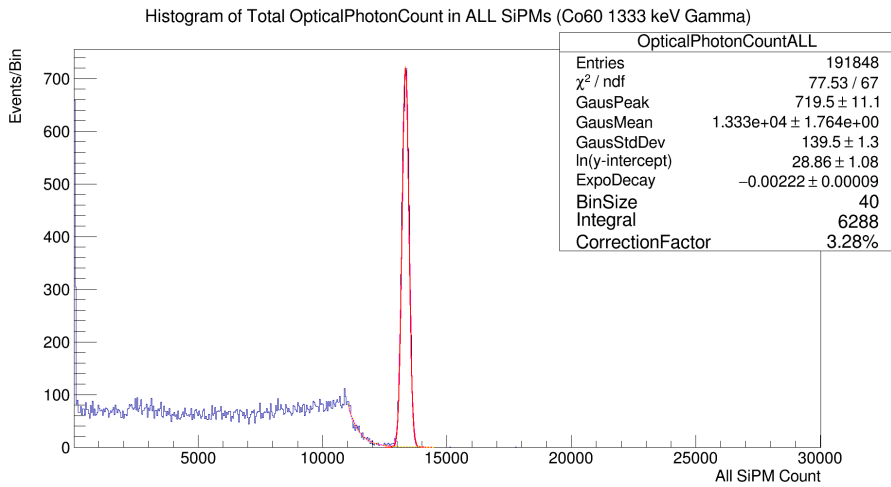


Figure 12: Simulated ^{60}Co 1333 keV decays with X-ray logic triggering on the 1173 keV gamma.

4. Results

4.1. Definition of Efficiency

We are using efficiency to mean the ratio of gamma rays that produce a full energy deposit in the detector to gamma rays that were expected to produce a full energy deposit in the detector according to simulations.

$$\mathbf{Efficiency} = \frac{\mathbf{Detected}}{\mathbf{Expected}} \quad (1)$$

In this context, the number of detected gamma rays is the integral over the full energy capture peak that is characteristic of the known energy gammas that we are looking for. The number of expected gamma rays is given in Equation 2.

$$\mathbf{Expected} = \mathbf{CorrectionFactor} \cdot \mathbf{BranchingRatio} \cdot \mathbf{Triggers} \quad (2)$$

4.2. Results for Flight Detector using X-ray-Triggered Gamma Sources

For the flight detector with real sources we get results in the form of histograms of the integrated signals from both the X-ray detector and the flight detector. There are several important considerations to take into account to interpret these data. For the electron capture sources, ^{65}Zn and ^{54}Mn , the X-rays are low energy and therefore the signals are of similar size to a noise signal that is generated by the X-ray detector and/or the electronics. However, we can use a further discrimination technique in software to remove these noise events. Specifically, anytime a signal rises above a relatively low value but then crosses the voltage axis at zero within 20 ns, the event is removed from the data set. The noise removal technique applied to a run with no sources but triggering using the differential discriminator brought the noisy data set down from 3827 events down to just 32, a 99.2% reduction in noise events, see Figures 13 - 16. The resultant histograms formed from noise reduction are below, see Figures 17 & 19.

After noise reduction, the leftover data is fit with a Gaussian (the previous data was for a trial run specifically to determine the efficacy of the noise removal procedure). The Gaussian is integrated to determine the number of X-rays we are using as triggers.

For the case of ^{65}Zn , we saw 134004 X-rays in the X-ray detector. Using the branching ratio and the correction factor, we expected to see 2692 gamma

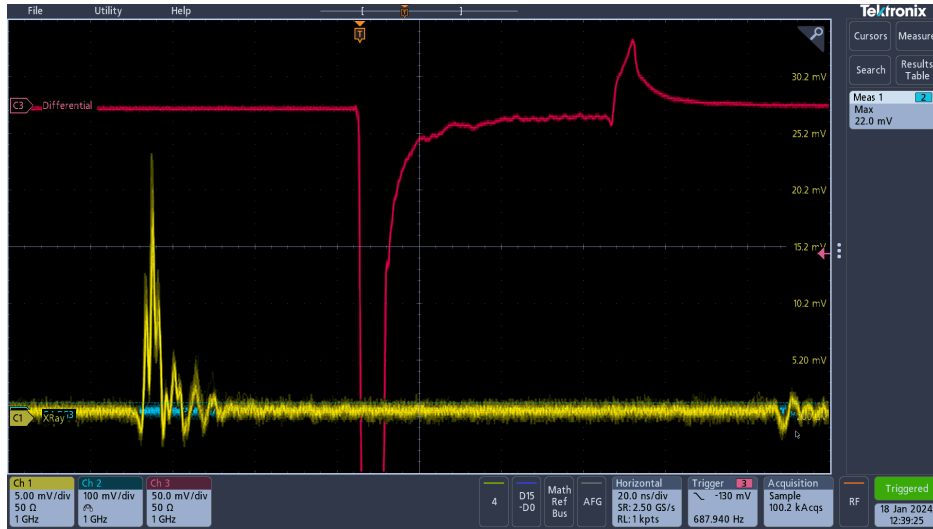


Figure 13: View of oscilloscope screen when triggering on the differential discriminator with no source. The noise events have a mostly consistent form and are much shorter in time than signals.

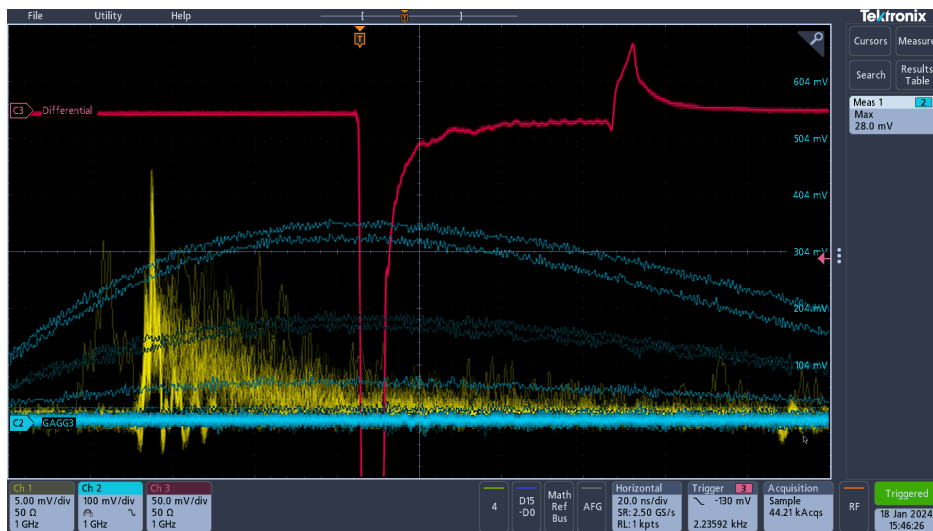


Figure 14: View of oscilloscope screen when triggering on the differential discriminator with the ^{65}Zn source in position. The blue traces are the GAGG signal and the two lines that peak at just above 304 mV are presumably the 1.115 MeV gammas.

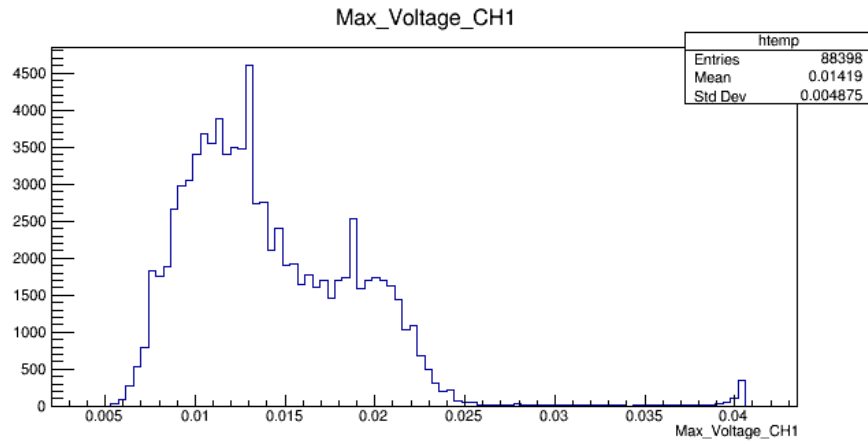


Figure 15: Data from ^{65}Zn before trimming.

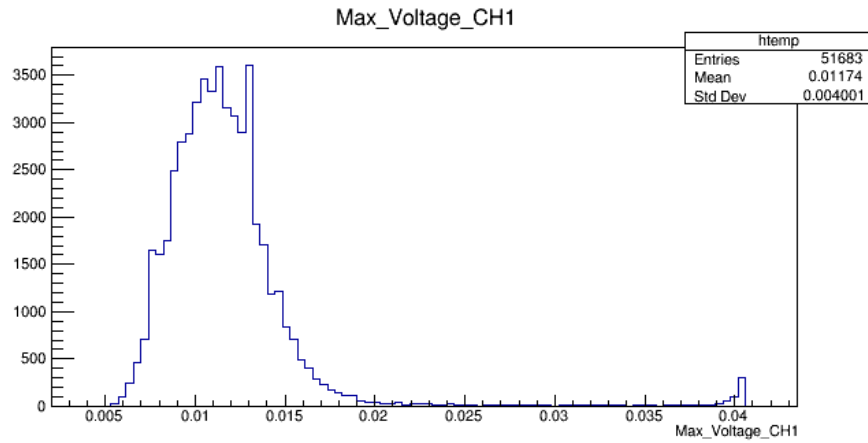


Figure 16: Data from ^{65}Zn after trimming. Note that the noise and the real signals are distinct.

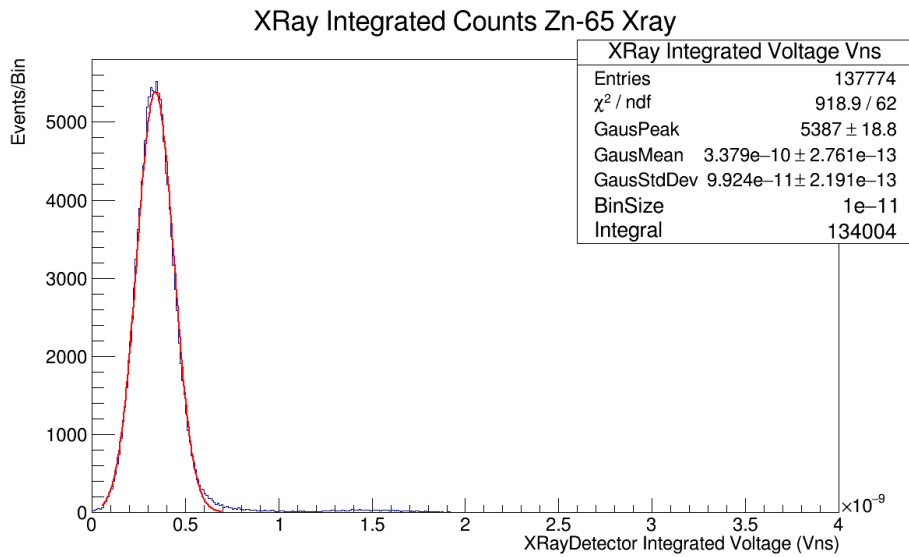


Figure 17: The 8 keV X-ray signals from ^{65}Zn in the X-ray detector.

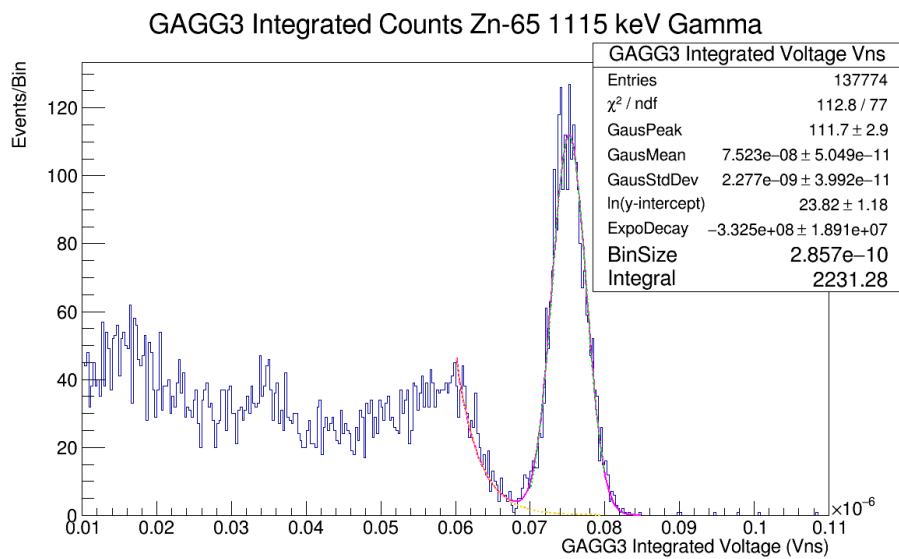


Figure 18: The 1115 keV gamma ray signals from ^{65}Zn in the flight detector.

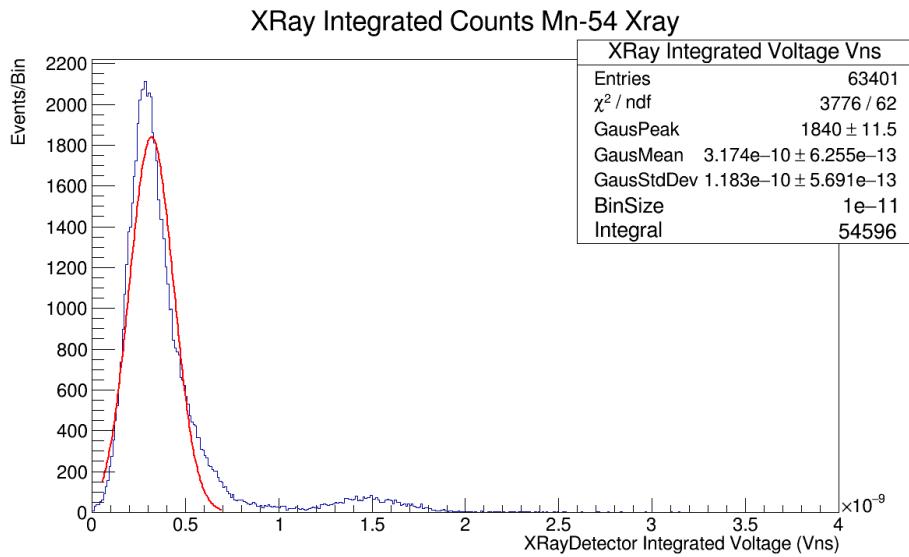


Figure 19: The 5.5 keV X-ray signals from ^{54}Mn in the X-ray detector.

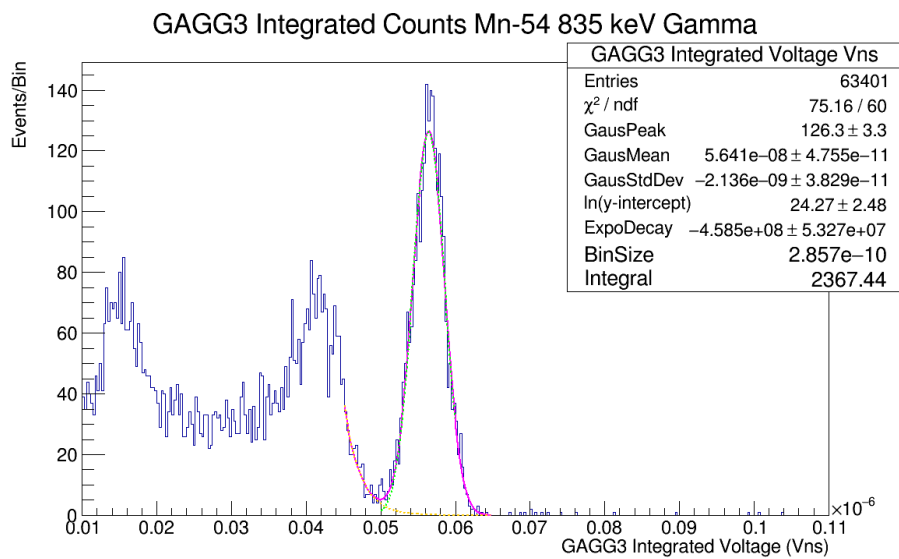


Figure 20: The 835 keV gamma ray signals from ^{54}Mn in the flight detector.

rays in the GAGG detector. The integral over the GAGG detector data gave 2231 gamma rays, thus an efficiency of 82.9%.

For ^{54}Mn , we saw 54596 X-rays in the X-ray detector using the integral over the Gaussian. Using the correction factor of 5.60%, we expected to see 3057 gammas in the GAGG detector. The integrated GAGG signal gave 2367 gammas, thus the efficiency is 77.4%

4.3. Results for Flight Detector using Annihilation-Triggered Gamma Sources

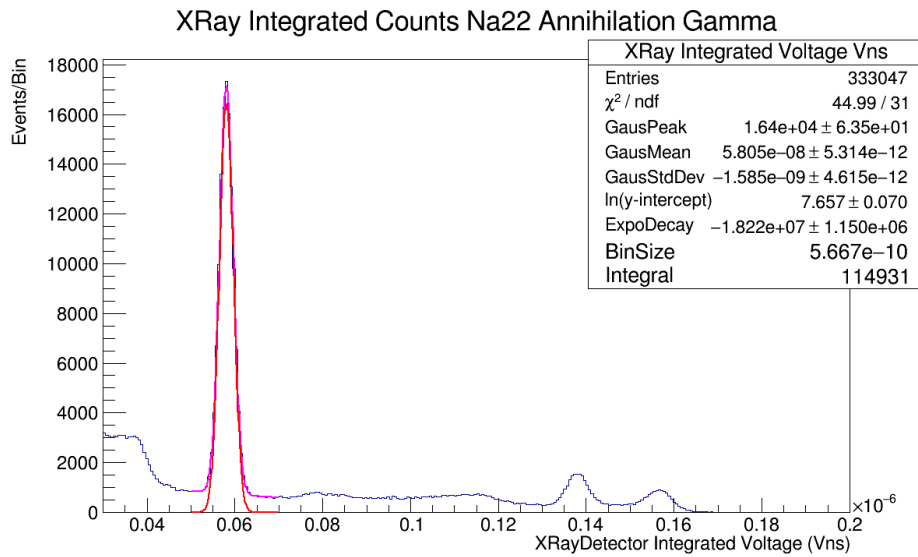


Figure 21: The 511 keV annihilation signal from ^{22}Na in the X-ray detector.

For ^{22}Na , we saw 114931 positron annihilation gammas in the X-ray detector using the integral over the Gaussian. The branching ratio for the 1274 keV nuclear de-excitation gamma is actually 200% in this context since there is a 100% branching ratio for the gamma with respect to positron emission and each annihilation produces 2 gammas. Thus, using the correction factor of 2.03%, we expected to see 4666 gammas in the GAGG detector. The integrated GAGG signal gave 4210 gammas, thus the efficiency is 90.2%. In the case of ^{22}Na , there is also the case where both the 1274 keV de-excitation gamma and one of the 511 keV positron annihilation gammas interact in the detector with a full energy deposit. The correction factor for this case is 0.69% and thus the predicted number of combined gamma signals is 793. We saw 721 gammas in the GAGG, or an efficiency of 90.9%.

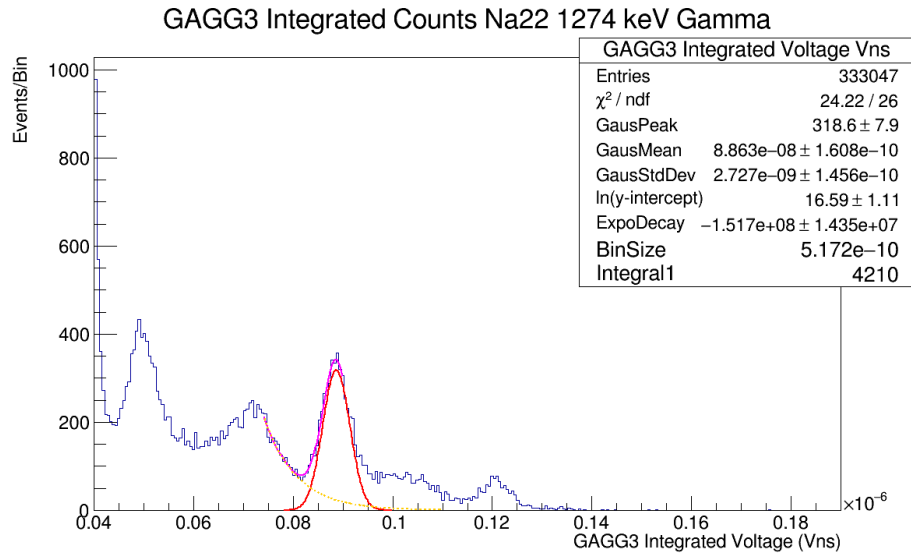


Figure 22: The 1274 keV de-excitation gamma signal from ^{22}Na in the flight detector.

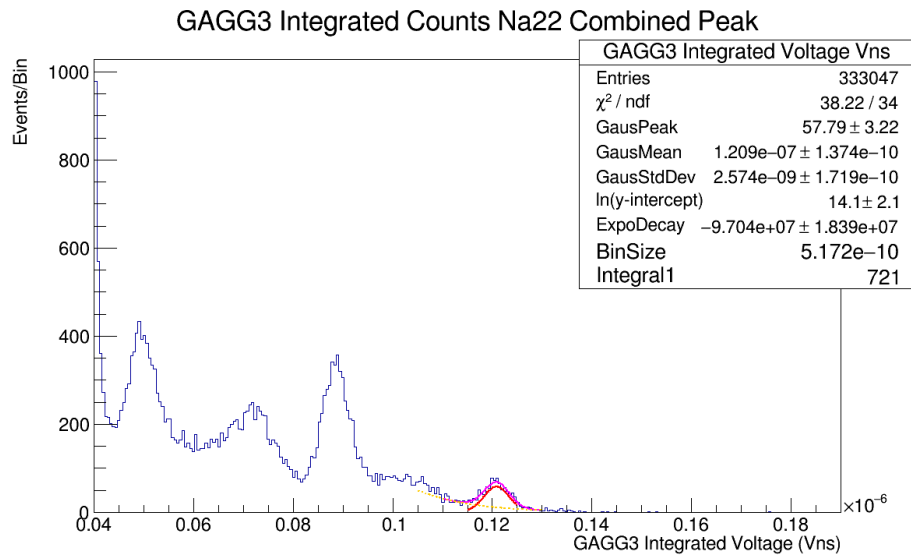


Figure 23: The 1785 keV combined peak signal from both the annihilation and de-excitation gammas of ^{22}Na in the flight detector.

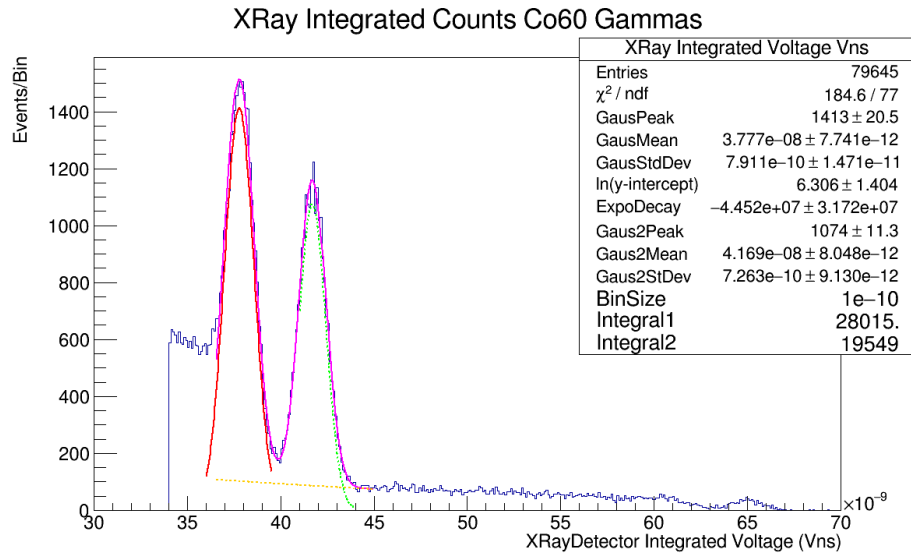


Figure 24: The ^{60}Co gamma peaks from the X-ray Detector.

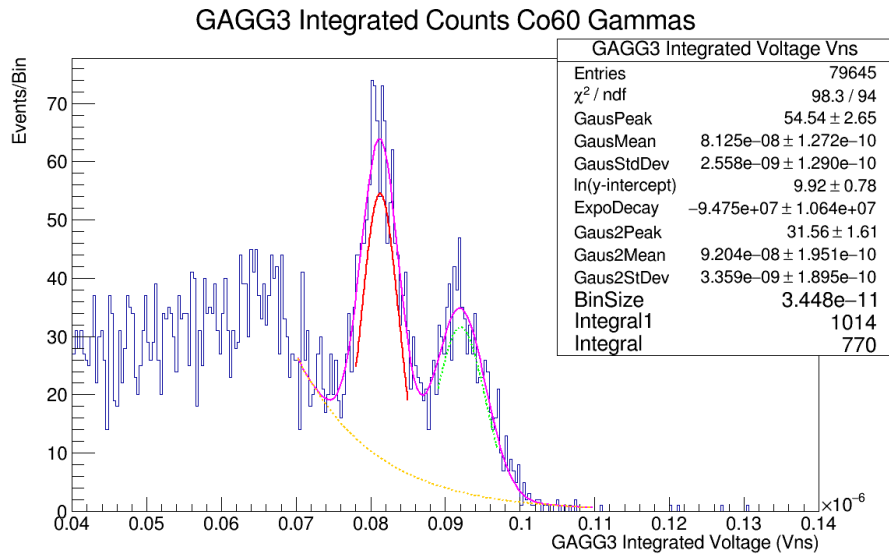


Figure 25: ^{60}Co gamma peaks from the GAGG flight detector. This is the unrestricted data set.

4.4. Results for Flight Detector Using a Gamma Cascade

^{60}Co has 2 close gamma rays (hereafter referred to as gamma 1 and gamma 2, since both the energy and position in the cascade are ordered in an increasing fashion), so care must be taken not to trigger on the Compton edge of gamma 2 when looking for gamma 2 using gamma 1 as a trigger. The full data set is included as well as data sets that have been cut in software to select for only the appropriate region of the data.

We used the uncut data to determine the number of X-rays and therefore the number of expected gammas. From the double Gaussian fit, we saw 28015 of gamma 1 and 19549 of gamma 2 detected in the X-ray detector. From this we expected 740 of gamma 1 and 919 of gamma 2 in the flight detector.

Naively using the uncut data, we saw 1014 of gamma 1 and 770 of gamma 2. This is clearly suspicious since this would have made the detector over 100% efficient for the detection of gamma 1. However, using the cut data sets, we saw only 676 gamma 1 and 761 gamma 2, meaning an efficiency 91.4% and 82.8% respectively.

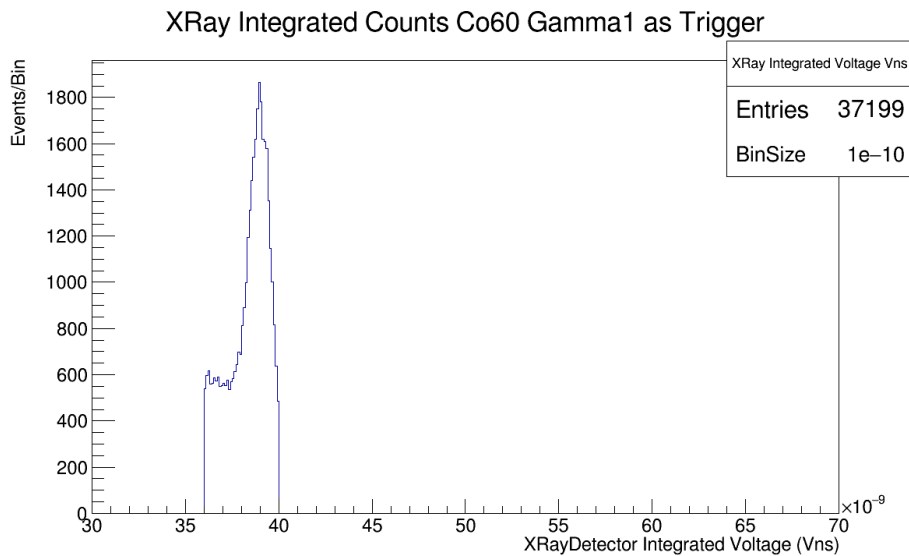


Figure 26: Data from ^{60}Co . (Left) Data restricted to the range corresponding to full energy deposits of gamma 1 in the X-ray detector.

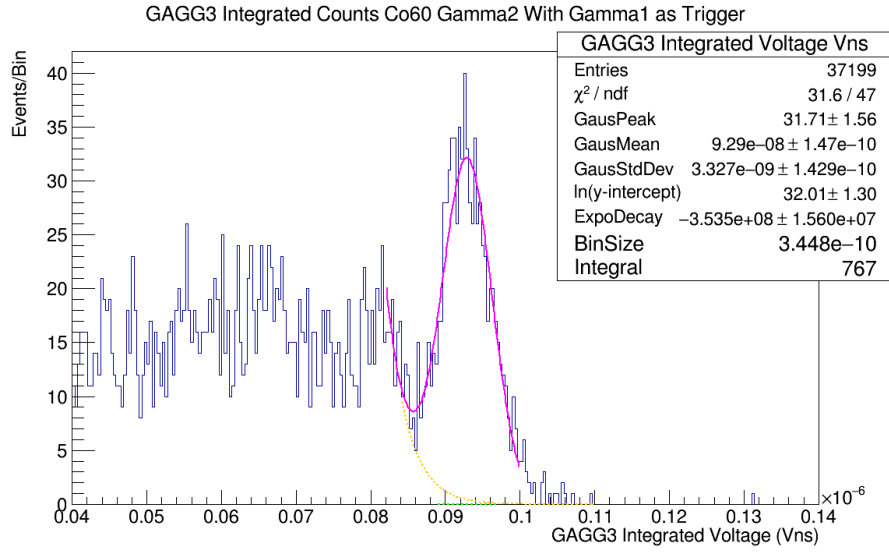


Figure 27: Data from ^{60}Co . The events in the GAGG detector when the data is restricted to gamma 1 triggers in the X-ray detector.

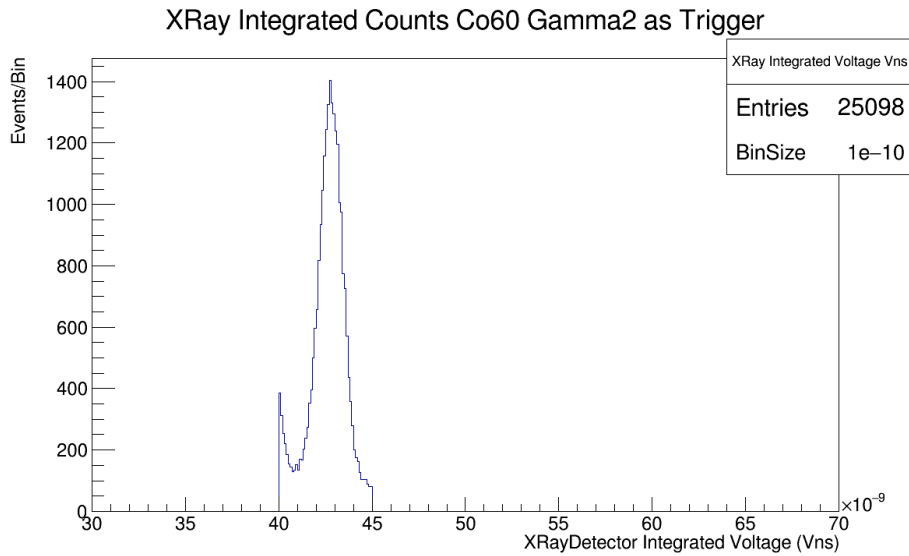


Figure 28: Data from ^{60}Co . Data restricted to the range corresponding to full energy deposits of gamma 2 in the X-ray detector.

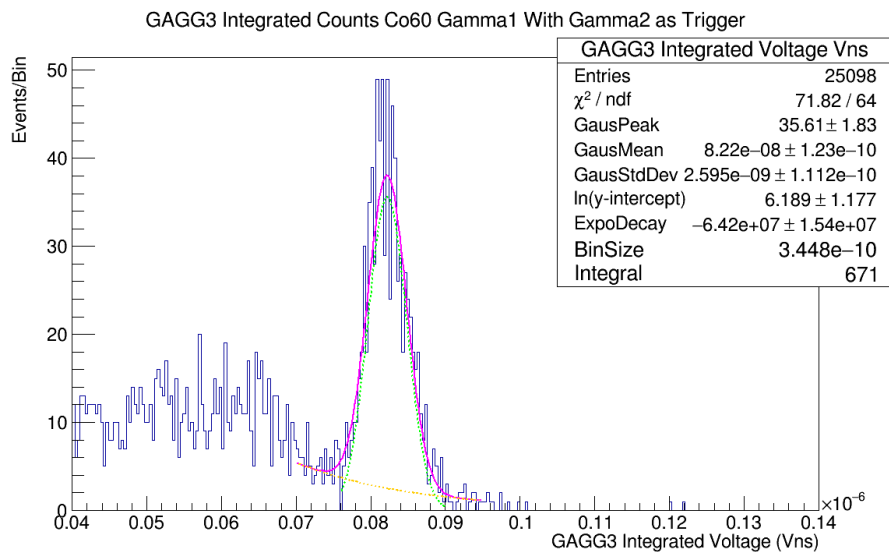


Figure 29: Data from ^{60}Co . The events in the GAGG detector when the data is restricted to gamma 2 triggers in the X-ray detector.

Table 2: The final efficiency measurement for the flight detector without uncertainties.

Source	Energy	Efficiency
^{65}Zn	1115 keV	82.9%
^{54}Mn	835 keV	77.4%
^{22}Na	1274 keV	90.2%
^{22}Na	1785 keV	90.9%
^{60}Co	1173 keV	91.4%
^{60}Co	1333 keV	82.8%

5. Uncertainties

5.1. Statistical Uncertainties

5.1.1. Statistical Uncertainties in measurement

For both the detected and expected values, we use the uncertainties in the fit parameters to determine the statistical uncertainties by integrating over the parameters with their values adjusted by their $1\text{-}\sigma$ uncertainties.

In the case of ^{65}Zn we see a $1\text{-}\sigma$ range of detected X-rays from 133243 to 134738, a fractional uncertainty of -0.57% and $+0.55\%$. While the $1\text{-}\sigma$ range in the detected gammas in the flight detector is from 2135 to 2330, a fractional uncertainty of -4.30% and $+4.43\%$.

In the case of ^{54}Mn , we see a $1\text{-}\sigma$ range of detected X-rays from 53946 to 55135, a fractional uncertainty of -1.19% and $+0.99\%$. While the $1\text{-}\sigma$ in the number of 835 keV gamma rays in the flight detector ranges from 2264 to 2472, a fractional uncertainty of -4.35% and $+4.44\%$.

For the ^{22}Na annihilation gammas in the X-ray detector, the $1\text{-}\sigma$ range is from 111280 to 118783, a fractional uncertainty of -3.18% and $+3.35\%$. In the flight detector, the number of detected 1274 keV gammas has a $1\text{-}\sigma$ range from 3885 to 4546, a fractional uncertainty of -7.72% and $+7.98\%$. The $1\text{-}\sigma$ range in the combined peak is from 635 to 812, a fractional uncertainty of -11.9% and $+12.6\%$.

In the case of ^{60}Co and specifically for triggering on gamma 1, the $1\text{-}\sigma$ range in the number of detected gammas in the X-ray detector is from 27100 to 28955, a fractional uncertainty of -3.27% and $+3.36\%$. For the data set that is restricted to gamma 1 triggers in the X-ray detector, the $1\text{-}\sigma$ range in detected gamma 2 in the flight detector is from 698 to 839, a fractional uncertainty of -9.00% and $+9.39\%$.

For the ^{60}Co triggering on gamma 2 in the X-ray detector, the $1\text{-}\sigma$ range in the number of detected gamma in the X-ray detector is from 19104 to 20007, a fractional uncertainty of -2.28% and $+2.34\%$. For the signal in the flight detector when restricted to this data set, the $1\text{-}\sigma$ range in the number of detected gamma 1 is from 610 to 737, a fractional uncertainty of -9.09% and $+9.84\%$.

5.1.2. Statistical Uncertainties in Simulation

We use the same technique of integrating over the lowest and highest case of fit parameters to obtain the $1\text{-}\sigma$ bounds on the correction factor for each simulation.

For ^{65}Zn 1115 keV gamma ray the $1\text{-}\sigma$ range in the number of full energy deposits is from 15847 to 16254, a fractional uncertainty of -0.96% and $+1.58\%$.

For ^{54}Mn 835 keV gamma ray the $1\text{-}\sigma$ range in the number of full energy deposits is from 22083 to 22669, a fractional uncertainty of -1.34% and $+1.28\%$.

For ^{22}Na 1274 keV gamma ray the $1\text{-}\sigma$ range in the number of full energy deposits is from 6783 to 7172, a fractional uncertainty of -2.77% and $+2.73\%$.

For ^{22}Na combined peak of 1785 keV the $1\text{-}\sigma$ range in the number of full energy deposits is from 2276 to 2498, a fractional uncertainty of -4.65% and $+4.65\%$.

For ^{60}Co 1173 keV gamma ray the $1\text{-}\sigma$ range in the number of full energy deposits is from 7117 to 7453, a fractional uncertainty of -2.27% and $+2.35\%$.

For ^{60}Co 1333 keV gamma ray the $1\text{-}\sigma$ range in the number of full energy deposits is from 6135 to 6446, a fractional uncertainty of -2.43% and $+2.51\%$.

5.2. Systematic Uncertainties

The main systematic uncertainty for most of the runs performed is going to be uncertainties in the position of the source. Simulations were done with a ^{65}Zn disk source that placed it in extreme positions relative to the measured position of the source in the lab. Specifically, an offset position with the source moved diagonally 4mm in the x-y plane, and 2 positions dubbed near and far that move the source 1 mm closer and further respectively.

In the lab the flight detector remains fixed, while the X-ray detector is on a stand that remains mostly at a constant height and the entire stand is slid in and out of position, making 1 mm a rather large amount of variation in height, perhaps larger than a $1\text{-}\sigma$ error. The offset simulation changes the correction factor of the ^{65}Zn source from 4.00% to 3.88% , a fractional uncertainty of 2.9% . The near and far simulations change the correction factor from 4.00% to 4.22% and 3.74% respectively, a fractional uncertainty of $+5.5\%$ and -6.5% respectively. The uncertainty from position in the actual lab is estimated to be largely due to the small height variations of about 1mm as opposed to lateral position variations of about a few mm, thus the systematic uncertainty is estimated to be about $+5.5\%$ and -6.5% .

There are known potential systematic effects that have been investigated and confirmed to be a minuscule correction such as angular correlation of the ^{60}Co gamma cascade, and the dimensions of the source disk. The solid angle of both the logic trigger volume and the simulated flight detector are both

very large from the perspective of the source and so the angular correlations in the gamma cascade are integrated over the solid angles to produce no correlation. As for the dimensions of the source, doubling the radius of the cylindrical disk source produced no significant impact on the correction factor in simulation as well as making the source 10 times thicker.

5.3. Total Uncertainty

The combined statistical uncertainty, assuming the 3 sources of statistical uncertainty are independent (simulated correction factor, measured triggers in X-ray detector, detected gammas in flight detector), is calculated for each source in the table below [3].

Table 3: The fractional total uncertainties for each source. In order: The source, the energy of the gamma, the statistical uncertainty in the correction factor from simulation, the statistical uncertainty in the number of triggers in the X-ray detector, the statistical uncertainty in the number of detected gammas in the flight detector, the estimated systematic uncertainty for each run, and the final combined statistical uncertainty.

Source	Energy	CF- σ	TRIG- σ	GAGG- σ	SYST- σ	TOTAL- σ
⁶⁵ Zn	1115 keV	+1.58%	+0.55%	+4.43%	+5.5%	+12.1%
		-0.96%	-0.57%	-4.30%	-6.5%	-12.3%
⁵⁴ Mn	835 keV	+1.28%	+0.99%	+4.44%	+5.5%	+12.2%
		-1.34%	-1.19%	-4.35%	-6.5%	-13.4%
²² Na	1274 keV	+2.73%	+3.35%	+7.98%	+5.5%	+19.5%
		-2.77%	-3.18%	-7.72%	-6.5%	-20.2%
²² Na	1785 keV	+4.65%	+3.35%	+12.6%	+5.5%	+26.1%
		-4.65%	-3.18%	-11.9%	-6.5%	-26.2%
⁶⁰ Co	1173 keV	+2.35%	+2.34%	+9.84%	+5.5%	+20.0%
		-2.27%	-2.28%	-9.09%	-6.5%	-20.1%
⁶⁰ Co	1333 keV	+2.51%	+3.36%	+9.39%	+5.5%	+20.8%
		-2.43%	-3.27%	-9.00%	-6.5%	-21.2%

6. Conclusion

The final result for a GAGG scintillator absolute efficiency measurement for the flight detector including uncertainties is summarized in Table 4. These three tagged gamma ray techniques of X-ray triggered gamma, annihilation triggered gamma, and gamma cascades are a valuable absolute efficiency method that can be used for other scintillating detectors when necessary.

7. Acknowledgements

Funding statement in progress

Table 4: The final efficiency result for the flight detector with total uncertainty.

Source	Energy	Efficiency	Uncertainty
^{65}Zn	1115 keV	82.9%	+12.1% -12.3%
^{54}Mn	835 keV	77.4%	+12.2% -13.4%
^{22}Na	1274 keV	90.2%	+19.5% -20.2%
^{22}Na	1785 keV	90.9%	+26.1% -26.2%
^{60}Co	1173 keV	91.4%	+20.0% -20.1%
^{60}Co	1333 keV	92.8%	+20.8% -21.2%

Funding: This work was supported by the NASA NIAC Program [grant numbers 80NSSC2K1900, 80NSSC18K0868, 80NSSC19M0971]; MSFC CAN [grant number 80MSFC18M0047]; Wichita State University MURPA; NASA EPSCoR PDG.

References

- [1] N. Solomey, J. Folkerts, H. Meyer, C. Gimar, J. Novak, B. Doty, T. English, L. Buchele, A. Nelsen, R. McTaggart, M. Christl, Concept for a space-based near-solar neutrino detector, Nuclear Instruments and Methods in Physics Research Section A: Accelerators, Spectrometers, Detectors and Associated Equipment 1049 (2023) 168064. doi:<https://doi.org/10.1016/j.nima.2023.168064>.
URL <https://www.sciencedirect.com/science/article/pii/S0168900223000542>
- [2] J. N. Bahcall, Gallium solar neutrino experiments: Absorption cross sections, neutrino spectra, and predicted event rates, Phys. Rev. C 56 (1997) 3391–3409. doi:[10.1103/PhysRevC.56.3391](https://doi.org/10.1103/PhysRevC.56.3391).
URL <https://link.aps.org/doi/10.1103/PhysRevC.56.3391>
- [3] G. Graham, N. Solomey, Y. Wah, E. Zimmerman, M. Daum, Y. Hsiung, J. Krider, E. Ramberg, Design and test results of a transition radiation detector for a fermilab fixed target rare kaon decay experiment, Nuclear Instruments and Methods in Physics Research Section A: Accelerators, Spectrometers, Detectors and Associated Equipment 367 (1) (1995) 224–227, proceedings of the 7th International Wire Chamber Conference. doi:[https://doi.org/10.1016/0168-9002\(95\)00537-4](https://doi.org/10.1016/0168-9002(95)00537-4).

URL [https://www.sciencedirect.com/science/article/pii/0168900295005374](https://www.sciencedirect.com/science/article/pii/S0168900295005374)

- [4] R. Brun, F. Rademakers, P. Canal, A. Naumann, O. Couet, L. Moneta, V. Vassilev, S. Linev, D. Piparo, G. GANIS, B. Bellenot, E. Guiraud, G. Amadio, wverkerke, P. Mato, TimurP, M. Tadel, wlv, E. Tejedor, J. Blomer, A. Gheata, S. Hageboeck, S. Roiser, marsupial, S. Wunsch, O. Shadura, A. Bose, CristinaCristescu, X. Valls, R. Isemann, root-project/root: v6.18/02 (Jun. 2020). doi:10.5281/zenodo.3895860. URL <https://doi.org/10.5281/zenodo.3895860>
- [5] J. Allison, K. Amako, J. Apostolakis, H. Araujo, P. Arce Dubois, M. Asai, G. Barrand, R. Capra, S. Chauvie, R. Chytracsek, G. Cirrone, G. Cooperman, G. Cosmo, G. Cuttone, G. Daquino, M. Donszelmann, M. Dreschel, G. Folger, F. Foppiano, J. Generowicz, V. Grichine, S. Guatelli, P. Gumplinger, A. Heikkinen, I. Hrivnacova, A. Howard, S. Incerti, V. Ivanchenko, T. Johnson, F. Jones, T. Koi, R. Kokoulin, M. Kossov, H. Kurashige, V. Lara, S. Larsson, F. Lei, O. Link, F. Longo, M. Maire, A. Mantero, B. Mascialino, I. McLaren, P. Mendez Lorenzo, K. Minamimoto, K. Murakami, P. Nieminen, L. Pandola, S. Parlati, L. Peralta, J. Perl, A. Pfeiffer, M. Pia, A. Ribon, P. Rodrigues, G. Russo, S. Sadilov, G. Santin, T. Sasaki, D. Smith, N. Starkov, S. Tanaka, E. Tcherniaev, B. Tome, A. Trindade, P. Truscott, L. Urban, M. Verderi, A. Walkden, J. Wellisch, D. Williams, D. Wright, H. Yoshida, Geant4 developments and applications, IEEE Transactions on Nuclear Science 53 (1) (2006) 270–278. doi:10.1109/TNS.2006.869826.
- [6] S. Agostinelli, J. Allison, K. Amako, J. Apostolakis, H. Araujo, P. Arce, M. Asai, D. Axen, S. Banerjee, G. Barrand, F. Behner, L. Bellagamba, J. Boudreau, L. Broglia, A. Brunengo, H. Burkhardt, S. Chauvie, J. Chuma, R. Chytracsek, G. Cooperman, G. Cosmo, P. Degtyarenko, A. Dell’Acqua, G. Depaola, D. Dietrich, R. Enami, A. Feliciello, C. Ferguson, H. Fesefeldt, G. Folger, F. Foppiano, A. Forti, S. Garelli, S. Giani, R. Giannitrapani, D. Gibin, J. Gómez Cadenas, I. González, G. Gracia Abril, G. Greeniaus, W. Greiner, V. Grichine, A. Grossheim, S. Guatelli, P. Gumplinger, R. Hamatsu, K. Hashimoto, H. Hasui, A. Heikkinen, A. Howard, V. Ivanchenko, A. Johnson, F. Jones, J. Kallenbach, N. Kanaya, M. Kawabata, Y. Kawabata, M. Kawaguti, S. Kelner, P. Kent, A. Kimura, T. Kodama, R. Kokoulin, M. Kossov,

H. Kurashige, E. Lamanna, T. Lampén, V. Lara, V. Lefebure, F. Lei, M. Liendl, W. Lockman, F. Longo, S. Magni, M. Maire, E. Medernach, K. Minamimoto, P. Mora de Freitas, Y. Morita, K. Murakami, M. Nagamatu, R. Nartallo, P. Nieminen, T. Nishimura, K. Ohtsubo, M. Okamura, S. O’Neale, Y. Oohata, K. Paech, J. Perl, A. Pfeiffer, M. Pia, F. Ranjard, A. Rybin, S. Sadilov, E. Di Salvo, G. Santin, T. Sasaki, N. Savvas, Y. Sawada, S. Scherer, S. Sei, V. Sirotenko, D. Smith, N. Starkov, H. Stoecker, J. Sulkimo, M. Takahata, S. Tanaka, E. Tcherniaev, E. Safai Tehrani, M. Tropeano, P. Truscott, H. Uno, L. Urban, P. Urban, M. Verderi, A. Walkden, W. Wander, H. Weber, J. Wellisch, T. Wenaus, D. Williams, D. Wright, T. Yamada, H. Yoshida, D. Zschesche, Geant4—a simulation toolkit, *Nuclear Instruments and Methods in Physics Research Section A: Accelerators, Spectrometers, Detectors and Associated Equipment* 506 (3) (2003) 250–303. doi:[https://doi.org/10.1016/S0168-9002\(03\)01368-8](https://doi.org/10.1016/S0168-9002(03)01368-8).
URL <https://www.sciencedirect.com/science/article/pii/S0168900203013688>

- [7] J. Allison, K. Amako, J. Apostolakis, P. Arce, M. Asai, T. Aso, E. Bagli, A. Bagulya, S. Banerjee, G. Barrand, B. Beck, A. Bogdanov, D. Brandt, J. Brown, H. Burkhardt, P. Canal, D. Cano-Ott, S. Chauvie, K. Cho, G. Cirrone, G. Cooperman, M. Cortés-Giraldo, G. Cosmo, G. Cuttone, G. Depaola, L. Desorgher, X. Dong, A. Dotti, V. Elvira, G. Folger, Z. Francis, A. Galoyan, L. Garnier, M. Gayer, K. Genser, V. Grichine, S. Guatelli, P. Guèye, P. Gumplinger, A. Howard, I. Hřivnáčová, S. Hwang, S. Incerti, A. Ivanchenko, V. Ivanchenko, F. Jones, S. Jun, P. Kaitaniemi, N. Karakatsanis, M. Karamitros, M. Kelsey, A. Kimura, T. Koi, H. Kurashige, A. Lechner, S. Lee, F. Longo, M. Maire, D. Mancusi, A. Mantero, E. Mendoza, B. Morgan, K. Murakami, T. Nikitina, L. Pandola, P. Paprocki, J. Perl, I. Petrović, M. Pia, W. Pokorski, J. Quesada, M. Raine, M. Reis, A. Ribon, A. Ristić Fira, F. Romano, G. Russo, G. Santin, T. Sasaki, D. Sawkey, J. Shin, I. Strakovsky, A. Taborda, S. Tanaka, B. Tomé, T. Toshito, H. Tran, P. Truscott, L. Urban, V. Uzhinsky, J. Verbeke, M. Verderi, B. Wendt, H. Wenzel, D. Wright, D. Wright, T. Yamashita, J. Yarba, H. Yoshida, Recent developments in geant4, *Nuclear Instruments and Methods in Physics Research Section A: Accelerators, Spectrometers, Detectors and Associated Equipment* 835 (2016) 186–225.

doi:<https://doi.org/10.1016/j.nima.2016.06.125>.

URL <https://www.sciencedirect.com/science/article/pii/S0168900216306957>